






# Global Biogeochemical Cycles®



## RESEARCH ARTICLE

10.1029/2021GB007055

## How Is the Ocean Anthropogenic Carbon Reservoir Filled?

Xabier Davila<sup>1</sup> , Geoffrey Gebbie<sup>2</sup>, Ailin Brakstad<sup>1</sup> , Siv K. Lauvset<sup>3</sup> , Elaine L. McDonagh<sup>3,4</sup> , Jörg Schwinger<sup>3</sup>, and Are Olsen<sup>1</sup> 

### Key Points:

- The cumulative anthropogenic carbon fluxes across the mixed-layer base over the industrialized era are derived from observations
- The subtropics, Southern Ocean and North Atlantic are the main conduits of anthropogenic carbon from the surface to the interior ocean
- The subtropics have been the most efficient regions in transporting anthropogenic carbon across the mixed layer per unit of volume

### Supporting Information:

Supporting Information may be found in the online version of this article.

### Correspondence to:

X. Davila,  
Xabier.Davila@uib.no

### Citation:

Davila, X., Gebbie, G., Brakstad, A., Lauvset, S. K., McDonagh, E. L., Schwinger, J., & Olsen, A. (2022). How is the ocean anthropogenic carbon reservoir filled? *Global Biogeochemical Cycles*, 36, e2021GB007055. <https://doi.org/10.1029/2021GB007055>

Received 5 MAY 2021  
Accepted 28 APR 2022

© 2022. The Authors.

This is an open access article under the terms of the [Creative Commons Attribution License](https://creativecommons.org/licenses/by/4.0/), which permits use, distribution and reproduction in any medium, provided the original work is properly cited.

<sup>1</sup>Geophysical Institute, University of Bergen, Bjerknæs Centre for Climate Research, Bergen, Norway, <sup>2</sup>Department of Physical Oceanography, Woods Hole Oceanographic Institution, Woods Hole, MA, USA, <sup>3</sup>Norwegian Research Centre (NORCE) AS, Bjerknæs Centre for Climate Research, Bergen, Norway, <sup>4</sup>National Oceanography Centre, Southampton, UK

**Abstract** About a quarter of the total anthropogenic CO<sub>2</sub> emissions during the industrial era has been absorbed by the ocean. The rate limiting step for this uptake is the transport of the anthropogenic carbon (C<sub>ant</sub>) from the ocean mixed layer where it is absorbed to the interior ocean where it is stored. While it is generally known that deep water formation sites are important for vertical carbon transport, the exact magnitude of the fluxes across the base of the mixed layer in different regions is uncertain. Here, we determine where, when, and how much C<sub>ant</sub> has been injected across the mixed-layer base and into the interior ocean since the start of the industrialized era. We do this by combining a transport matrix derived from observations with a time-evolving boundary condition obtained from already published estimates of ocean C<sub>ant</sub>. Our results show that most of the C<sub>ant</sub> stored below the mixed layer are injected in the subtropics (40.1%) and the Southern Ocean (36.0%), while the Subpolar North Atlantic has the largest fluxes. The Subpolar North Atlantic is also the most important region for injecting C<sub>ant</sub> into the deep ocean with 81.6% of the C<sub>ant</sub> reaching depths greater than 1,000 m. The subtropics, on the other hand, have been the most efficient in transporting C<sub>ant</sub> across the mixed-layer base per volume of water ventilated. This study shows how the oceanic C<sub>ant</sub> uptake relies on vertical transports in a few oceanic regions and sheds light on the pathways that fill the ocean C<sub>ant</sub> reservoir.

## 1. Introduction

Since the beginning of the industrial era, humankind has emitted large quantities of CO<sub>2</sub> to the atmosphere. This has changed its radiative properties and resulted in global warming. The increased atmospheric CO<sub>2</sub> concentration also drives ocean anthropogenic carbon (C<sub>ant</sub>) uptake, which mitigates the atmospheric CO<sub>2</sub> rise and consequently global warming. Although oceanic C<sub>ant</sub> is chemically indistinguishable from the large natural carbon pool of 38 000 Pg C (Sarmiento & Gruber, 2002), the total C<sub>ant</sub> inventory in the ocean has been constrained to within 15%. Various methods, based on the reconstruction of preindustrial ocean carbon concentrations, transient tracers, and optimized circulation models agree that the global ocean has absorbed one fourth of the total anthropogenic emissions from fossil fuel combustion, cement manufacturing, and land use change (DeVries, 2014; Khatiwala et al., 2009; McNeil et al., 2003; Sabine et al., 2004), that is, 160 ± 20 Pg C out of 655 ± 55 Pg C (Friedlingstein et al., 2020). These estimates of ocean C<sub>ant</sub> content and distribution are valuable for understanding climate sensitivity to CO<sub>2</sub> emissions, vulnerability of ocean carbon uptake for further climate change, for quantifying the extent of ocean acidification (Lauvset et al., 2020), as an independent check on estimates of the terrestrial sink of CO<sub>2</sub> (e.g., DeVries, 2014; Khatiwala et al., 2009), and for evaluation of Earth System Models (e.g., Liddicoat et al., 2021).

Ocean C<sub>ant</sub> uptake is regulated by an interaction of physical and chemical processes (Maier-Reimer & Hasselmann, 1987). The chemical processes control the mass of C<sub>ant</sub> that can be absorbed into the well-mixed upper ocean for a given rise in atmospheric CO<sub>2</sub> before equilibrium is reached. It is dependent on the water's buffer capacity, formally quantified as the Revelle factor, which expresses the relationship between changes in CO<sub>2</sub> partial pressure (pCO<sub>2</sub>) and Dissolved Inorganic Carbon (DIC) (Middelburg et al., 2020). A high Revelle factor means low buffer capacity and relatively low capacity for C<sub>ant</sub> uptake and vice versa for low Revelle factor. The physical processes control the extent to which waters that have absorbed C<sub>ant</sub> from the atmosphere are transported away from the well-ventilated upper ocean mixed layer to the deep ocean (Graven et al., 2012; Sarmiento et al., 1992) and replaced with older waters through upwelling. These older waters have not been exposed to the present atmosphere and thus provide the surface ocean with further capacity for C<sub>ant</sub> uptake. The ocean circulation thus ensures the ongoing absorption of C<sub>ant</sub> by the subduction of C<sub>ant</sub> across the mixed layer.

Some features of the  $C_{ant}$  subduction across the mixed-layer base are evident from the distribution of  $C_{ant}$  in the ocean, in particular, the large column inventories within and immediately downstream of deep and mode water formation regions. These include the North Atlantic, reflecting the  $C_{ant}$  transport by the North Atlantic Deep Water (NADW), and the Antarctic convergence and regions to the north of this, reflecting the  $C_{ant}$  transport by Antarctic Intermediate Water (AAIW) and Subantarctic Mode Water (SAMW) (Sabine et al., 2004). AAIW and SAMW are collectively referred to as MIW (Mode/Intermediate Water) in the remainder of this contribution. However, inventory estimates do not provide explicit information about these  $C_{ant}$  fluxes across the mixed-layer base. Instead, such anthropogenic carbon transports have been determined by combining  $C_{ant}$  estimates with geostrophic flow fields (e.g., Álvarez et al., 2003; Holfort et al., 1998; Lundberg & Haugan, 1996; Macdonald et al., 2003; Rosón et al., 2003) and by using data-based inverse methods (Mikaloff-Fletcher et al., 2006). These studies show that the  $C_{ant}$  that is taken up in the deep water formation regions in the Subpolar North Atlantic (i.e., Labrador and Nordic Seas) is transported southward by entrainment into the NADW. In the Southern Ocean, about half of the  $C_{ant}$  that is absorbed are transported equatorward mostly as a consequence of the spreading of the MIW (Mikaloff-Fletcher et al., 2006). The  $C_{ant}$  transported along these pathways is stored below the subtropical gyres, resulting in the high-column inventories observed there.

More sophisticated methods, such as transport matrices (offline ocean circulation models in the form of a matrix), have been used to provide the first 3D estimates of  $C_{ant}$  distribution (Khatiwala et al., 2009) and transport (DeVries, 2014; Khatiwala et al., 2013). Khatiwala et al. (2013) and DeVries (2014) used observationally optimized transport matrices to determine ocean  $C_{ant}$  uptake, transport, and storage. Their findings largely agree with those determined using the inverse methods described above; the large storage rates in the midlatitude oceans are a consequence of the equatorward flows of  $C_{ant}$  rich waters subducted in the Southern Ocean and Subpolar North Atlantic. The results provided by these methods are part of the cornerstones of oceanic  $C_{ant}$  studies; however, fluxes across the mixed-layer base were not estimated. Such fluxes across the base of the mixed layer and their spatial distribution have only been explored in models. Bopp et al. (2015) used the NEMO-PISCES model (Aumont & Bopp, 2006; Madec, 2008; Timmerman et al., 2005) to show that global subduction is dominated by the Southern Ocean and the subtropics. The subduction in the Southern Ocean was found to be a result of vertical mixing, while in the subtropics, it is a result of the interplay between the sloping mixed-layer base (horizontal mixed-layer base depth gradients) and lateral advection, including Ekman pumping. At high northern latitudes, vertical mixing was found to drive most of the subduction. Pathways of  $C_{ant}$  to the interior ocean were also explored by Iudicone et al. (2016) who applied a thermodynamic water-mass framework to output from the ORCA2-LIM-PISCES model (Aumont & Bopp, 2006; Madec et al., 1998; Timmerman et al., 2005) to identify the importance of various processes, in particular water mass transformation and diffusion, in transporting  $C_{ant}$  to the different density levels of the global ocean.

The overall aim here is to provide an observation-based estimate of the fluxes across the base of the mixed layer and the subsequent movement in the interior by identifying the oceanic regions that filled the ocean with  $C_{ant}$  over the time period 1780–2012. We do this by combining the Total Matrix Intercomparison (TMI) transport matrix (Gebbie & Huybers, 2012) with estimates of  $C_{ant}$  growth rates in the mixed layer, obtained from DeVries (2014). Unlike other transport matrices, the TMI matrix is constrained almost entirely from observations without relying on information from General Circulation Models (Khatiwala et al., 2013) or dynamical constraints (DeVries & Primeau, 2011). By combining a boundary Green's function derived from the TMI transport matrix with the time evolving  $C_{ant}$  boundary concentration, we estimate the total amount of  $C_{ant}$  injected across the mixed-layer base and into the interior ocean. We also apply a particular focus on deep regions (>1,000 m) both where and when the deep ocean  $C_{ant}$  was injected at surface.

## 2. Methods

$C_{ant}$  behaves as a conservative tracer (Sarmiento et al., 1992), and thus with a representation of ocean circulation and a boundary condition, the ocean transport of  $C_{ant}$  can be quantified. Green's functions reproduce the advective-diffusive pathways that connect the ocean surface with the interior and they have been widely used to assess the distribution of  $C_{ant}$  in the ocean (e.g., Khatiwala et al., 2009; Waugh et al., 2006). Here, we determine the subduction of  $C_{ant}$  across the ocean's mixed layer using the boundary Green's function from Gebbie and Huybers (2012) that encapsulates the ocean circulation and a  $C_{ant}$  boundary condition obtained from

DeVries (2014). The cumulative fluxes in each of the mixed-layer patches,  $F(s, t)$  (in mol), into the interior ocean locations,  $i$ , are given by

$$F(s, t) = \sum_{\tau=0}^{233} \sum_{i=0}^N g(s, i, \tau) c(s, t - \tau) \quad (1)$$

where  $g(s, i, \tau)$  represents the boundary propagator from the mixed-layer patch  $s$  to each of  $N = 57,514$  interior locations below the mixed layer and is here expressed in terms of volume (i.e., in  $\text{m}^3$ ). Overall, the ocean is discretized into a grid with a horizontal resolution of  $4^\circ$  by  $4^\circ$  and 33 vertical levels. The depth of the mixed layer varies regionally, such that the number of vertical levels in the mixed-layer patches (i.e., mixed-layer) also varies regionally. There are altogether 74,064 grid cells with 2,806 mixed-layer patches that contain 16,550 grid cells within the mixed layer (which is completely homogeneous). The boundary propagator  $g$  runs with a lag,  $\tau$ , up to 233 years. The volume that leaves the mixed-layer patch  $s$  is combined with the mixed-layer  $C_{ant}$  time histories  $c$  (in  $\text{mol m}^{-3}$ ) for times  $t = 1780\text{--}2012$ .

The  $C_{ant}$  boundary condition was obtained from the  $C_{ant}$  distribution estimated with the Ocean Circulation Inverse Model (OCIM) by DeVries (2014), which provides an appropriate representation of the  $C_{ant}$  concentrations by coupling an interactive atmosphere and an ocean transport matrix based on observational and dynamical constraints.

### 2.1. Boundary Green's Function

Here, we use the boundary Green's function determined by Gebbie and Huybers (2012). This contains the surface pattern of contributions ( $g(s, i, \tau)$  in Equation 1) to ocean's interior volume that arrive with a lag of  $\tau$  time steps. It was determined from modern-day tracer observations by constraining ocean-mixing pathways with the TMI and ventilation rates with  $^{14}\text{C}$ . The TMI is a water decomposition method based on the inversion of tracer conservation equations for six ocean properties (potential temperature ( $\theta$ ), salinity,  $\delta^{18}\text{O}_{sw}$ ,  $\text{PO}_4^{3-}$ ,  $\text{NO}_3^-$ , and  $\text{O}_2$ ) (Gebbie & Huybers, 2010). In essence, by identifying mixtures of water properties, the TMI diagnoses the pathways that connect 57,514 inner ocean boxes with 2,806 mixed-layer patches as explained above. For the ventilation rates, lags up to 2,000 years permit more than 99.9% of ocean's memory to be captured (Gebbie, 2012; Gebbie & Huybers, 2012). The TMI ocean circulation model is also used here as a forward model to estimate the distribution and inventory of  $C_{ant}$  in the ocean, which is used to examine model consistency (Section 2.3).

### 2.2. Mixed-Layer $C_{ant}$ Time History

The time history of  $C_{ant}$  in the mixed layer used as boundary condition  $c$  was extracted from the time and space resolving the global ocean  $C_{ant}$  (control “inversion” (CTL)) estimate published by DeVries (2014), which is based on the OCIM. Briefly, the OCIM is data-constrained dynamical circulation model, optimized by assimilating observations of  $\theta$ , salinity,  $^{14}\text{C}$  and CFC-11, as well as estimates of mean sea surface height and sea surface heat, and freshwater fluxes (DeVries, 2014; DeVries & Primeau, 2011). DeVries (2014) estimated the  $C_{ant}$  ocean distribution as the difference in ocean DIC between a time-varying run where the atmospheric  $p\text{CO}_2$  increases according to observations and a preindustrial run under a constant preindustrial atmospheric concentration of 280 ppm. He assumed that ocean biology and circulation remained constant since the preindustrial era. The OCIM  $C_{ant}$  distribution was supplied on a resolution of  $2^\circ$  by  $2^\circ$  and was interpolated onto the TMI grid ( $4^\circ$  by  $4^\circ$ ) to enable us to use it as a boundary condition.

### 2.3. Model Evaluation

To evaluate our approach, we propagate the OCIM mixed-layer  $C_{ant}$  concentration throughout the ocean interior. We derive a surface boundary flux  $f$ , equivalent to the yearly growth rate of the OCIM mixed-layer  $C_{ant}$  time history ( $c$  in Equation 1), and then force the TMI ocean circulation model (Section 2.1) according to the equation:

$$\frac{dC_{ant}}{dt} = LC_{ant} + Bf \quad (2)$$

where  $B$  is the matrix corresponding to the mixed layer that imposes the surface boundary flux  $f$  into the interior ocean transport matrix  $L$  (Gebbie & Huybers, 2012). The equation is solved by the timestepping algorithm “ode15s” in MATLAB. The boundary Green's function, the collection of  $g$ 's in Equation 1, is self-consistently produced with this method (see Appendix A in Gebbie, 2012). Thus, the extent to which the  $C_{ant}$  distribution and inventory determined using Equation 2 align with existing assessments provides insight on the fidelity of our results.

The total ocean  $C_{ant}$  inventory determined from the TMI for 2010 is 178 Pg C (Figure 1a). This is close to the recent inventory estimates by Khatiwala et al. (2013) and DeVries (2014) who estimated  $155 \pm 31$  and 155–160 Pg C, respectively. In this study, we focus on the fluxes across the base of the mixed layer, and the reproduction of the inventory provides an insight of the suitability of the circulation model for that purpose. Given that the true size of the ocean carbon inventory is not known, and that our  $C_{ant}$  concentration in the mixed layer is not independently constrained, our approach cannot be used to provide an independent estimate of the inventory.

Differences between the TMI column inventory distribution (Figure 1b) and the one presented by DeVries (2014) (Figure 1c) are solely due to differences in circulation. In general, the distribution of  $C_{ant}$  derived from the TMI aligns with other estimates (DeVries, 2014; Khatiwala et al., 2013). The Labrador and Nordic Seas contain large amounts of  $C_{ant}$  up to  $90 \text{ mol m}^{-2}$ , while the smallest column inventories are found in the Southern Ocean, south of the Polar Front. This region is dominated by upwelling of old waters from the Antarctic Circumpolar Current with low concentrations of  $C_{ant}$ . In the Subpolar and Subtropical North Atlantic, the TMI-derived estimates are about 66% and 69% of the OCIM-derived ones, respectively. Specifically, while the OCIM results show large inventories in the west associated with the Deep Western Boundary Current, this feature is much less strong in the TMI results, indicating more diffusive transports in the latter. The largest disagreement in terms of total inventory occurs in the tropical Pacific, where, when integrated over the large volume of the basin, the slightly higher concentrations in the TMI amount to a difference of 10.8 Pg C (Figure 1d). The column inventories in the Arctic are slightly higher likely as a consequence of poor constraints on its circulation rates due to the dearth of  $^{14}\text{C}$  data from this region at the time the TMI analyses were carried out (Gebbie & Huybers, 2012).

The zonally integrated cross sections (Figure 2) shed light on which water masses contribute most to these differences. The deepest penetration of  $C_{ant}$  comes from the NADW in the North Atlantic due to the contributions of the Labrador Sea Water (LSW;  $\sim 1,000 \text{ m}$  north of  $40^\circ\text{N}$ ) and the deep convection in the Nordic Seas (north of  $60^\circ\text{N}$ ) that transport  $C_{ant}$  concentrations of  $\sim 30 \text{ } \mu\text{mol kg}^{-1}$ . In the Atlantic, Pacific, and Indian Ocean basins, the Southern Hemisphere MIW propagates  $C_{ant}$  down to 1,000 m and northward, resulting in high concentrations in the main thermocline below the subtropical gyres. The largest disagreement with the OCIM, up to  $20 \text{ } \mu\text{mol kg}^{-1}$  less, appears throughout the North Atlantic water column between  $30$  and  $50^\circ\text{N}$  and is the deep expression of the differences in the Deep Western Boundary Current discussed above. Further, concentrations in the deep Nordic Seas are at least  $15 \text{ } \mu\text{mol kg}^{-1}$  larger in the TMI than in the OCIM. We note, however, that the TMI-derived Nordic Seas inventory of  $\sim 70 \text{ mol m}^{-2}$  and  $\sim 1.3 \text{ Pg C}$  for 2002 (not shown) agrees with previous estimates of  $\sim 70 \text{ mol m}^{-2}$  and  $0.9\text{--}1.4 \text{ Pg C}$  (Olsen et al., 2010) for the same year, whereas the OCIM estimate is  $\sim 60 \text{ mol m}^{-2}$  and about  $1.2 \text{ Pg C}$ , which renders confidence to the TMI approach here. In the equatorial thermocline in all ocean basins, the concentrations are about  $20 \text{ } \mu\text{mol kg}^{-1}$  higher in the TMI-derived estimates.

The difference between the TMI and OCIM  $C_{ant}$  inventory results from the differences in the circulation field partially due to the different set of ocean tracers used to constrain the mixing pathways and ventilation rates in the OCIM and TMI. First, the rates in the OCIM are constrained by CFC-11 and  $^{14}\text{C}$ , while the TMI only uses  $^{14}\text{C}$ . Due to its long half-life (5,730 years),  $^{14}\text{C}$  data are suitable to resolve ventilation rates on a long timescale, whereas CFCs, being much more modern, resolve decadal to multidecadal timescales (England & Maier-Reimer, 2001). This long half-life likely results in the concentration differences in the North Atlantic, which we believe are more trustworthy in the OCIM. The Deep Western Boundary Current is sharp in the OCIM, while it appears more diffuse in the TMI likely due to the dependency of the  $^{14}\text{C}$  alone that might not be sufficient to resolve the near-present circulation in the latter. Second, the additional nutrient and oxygen tracers in the TMI could constrain uncertain biogeochemical fluxes (DeVries & Primeau, 2011; Schlitzer, 2004). In the equatorial regions, the TMI accumulates more  $C_{ant}$  than the OCIM: about  $10 \text{ } \mu\text{mol kg}^{-1}$  in the thermocline.  $\text{PO}_4^{3-}$  is among the tracers used to derive the pathways in the TMI, and the TMI corrects for remineralization under the assumption that the Anderson and Sarmiento (1994) stoichiometric ratios, 1:-170 P: $\text{O}_2$ , apply. Recently, Carter et al. (2021) determined that this ratio is likely smaller,  $1\text{--}141 \pm 12$ . The fixed stoichiometric ratios or

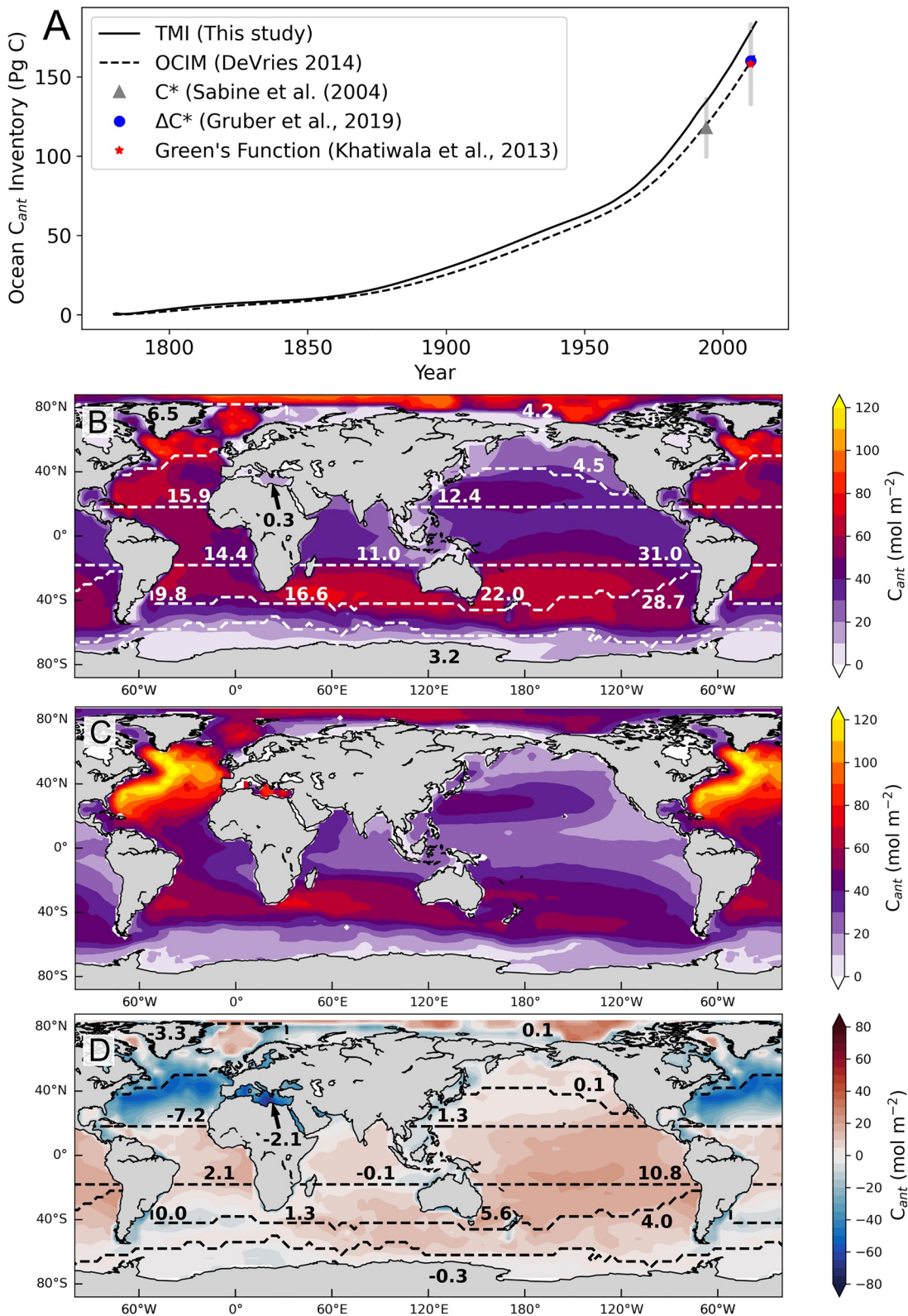
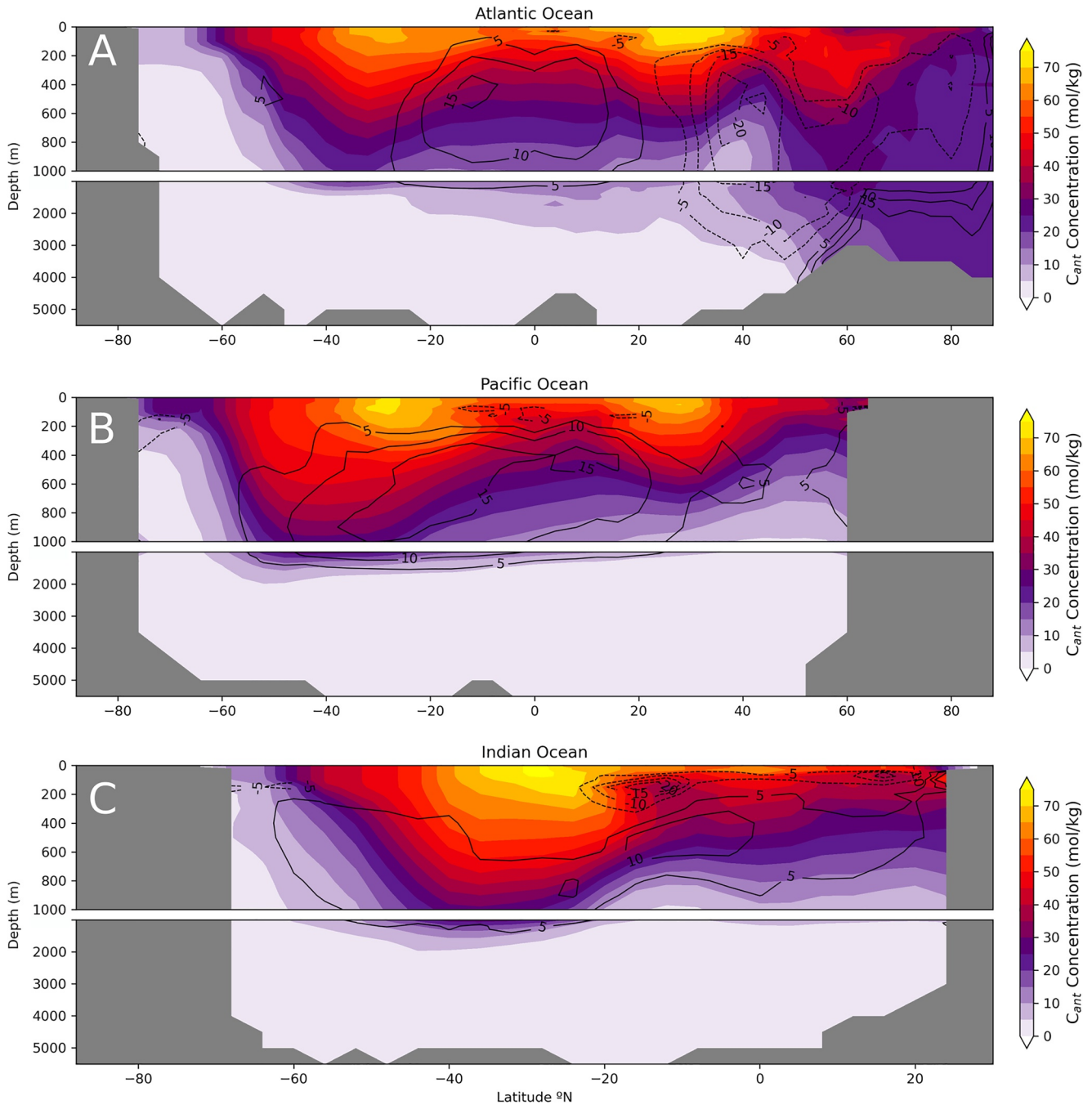
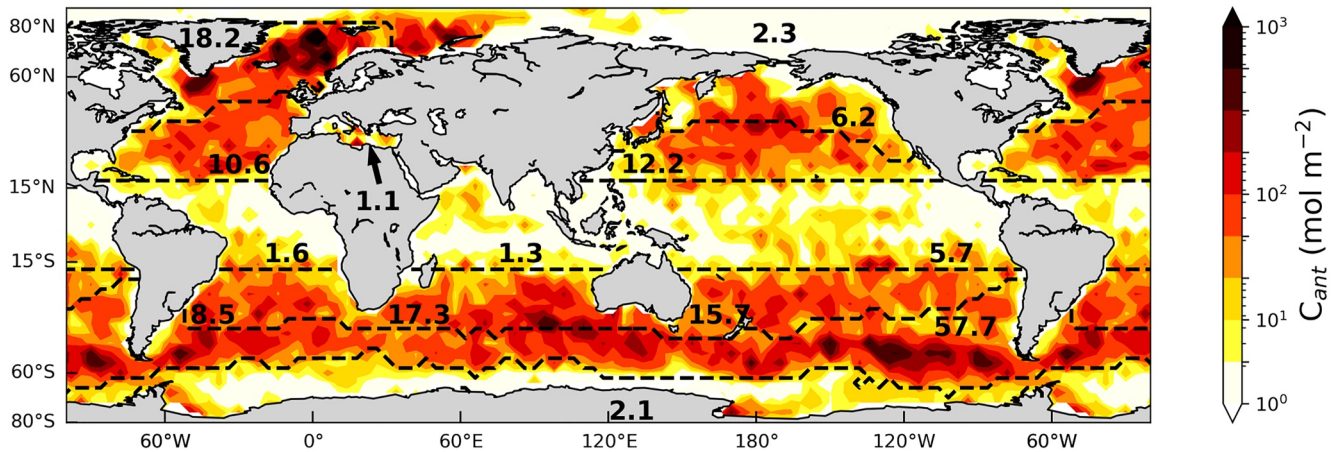


Figure 1.



**Figure 2.** Vertical distribution of  $C_{ant}$  zonally averaged, for (a) Atlantic, (b) Pacific, and (c) Indian Ocean for 2010. Black contours indicate the differences with Ocean Circulation Inverse Model (OCIM) for 2010 calculated as Total Matrix Intercomparison (TMI) minus OCIM, where solid lines mean higher and dashed lines lower concentrations in the TMI. The missing Greenland-Scotland Ridge in the Atlantic (60°N) is an artifact of the longitudinal averaging across the entire basin. Note difference in y axis (depth) scaling between 0–1,000 m and 1,000–5,000 m.

**Figure 1.** (a)  $C_{ant}$  inventory evolution produced by the Total Matrix Intercomparison (TMI) for 1780–2012 and estimates from the C\* method by Sabine et al. (2004), Green's Function by Khatiwala et al. (2009),  $\Delta C^*$  by Gruber et al. (2019), and Ocean Circulation Inverse Model (OCIM) by DeVries (2014). (b)  $C_{ant}$  column inventory produced by the TMI for 2010. (c)  $C_{ant}$  column inventory produced by the OCIM control “inversion” for 2010 (DeVries, 2014). (d) Differences between the OCIM and the TMI column inventory estimates for 2010 calculated as TMI minus OCIM; blue colors indicate lower and red higher inventories in the TMI. The OCIM field was interpolated onto the TMI grid. Dashed lines represent the outcrop areas of different water masses according to Gebbie and Huybers (2010). The values within each region indicate the total mass of  $C_{ant}$ .



**Figure 3.** Cumulative  $C_{ant}$  fluxes across the mixed-layer base for 1780–2012 from the boundary Green's function and  $C_{ant}$  boundary condition. Black-dashed lines define the various regions mentioned in the text and in Table 1, while the numbers indicate the total mass of  $C_{ant}$  injected within each region, in Pg C. The color scale is logarithmic.

**Table 1**  
Regional Injection and Inventory Below the Mixed Layer for 2012 in Pg C

Region	Injection	Inventory
<b>Arctic Ocean</b>	<b>2.3</b>	<b>4.2 (4.3)</b>
<b>Atlantic Ocean</b>	<b>49.8</b>	<b>41.9 (52.5)</b>
Labrador Sea	7.1	4.1 (5.2)
Nordic Seas	11.1	1.3 (1.6)
North Subtropical Atlantic	10.6	14.6 (16.4)
South Subtropical Atlantic	8.5	8.9 (10.1)
Tropical Atlantic	1.6	14.0 (14.9)
Subantarctic Atlantic	10.9	3.4 (4.3)
<b>Pacific Ocean</b>	<b>77.7</b>	<b>80.6 (91.8)</b>
Subpolar North Pacific	6.2	3.9 (4.6)
North Subtropical Pacific	12.2	11.2 (12.8)
South Subtropical Pacific	15.7	20.1 (22.7)
Tropical Pacific	5.7	29.5 (32.1)
Subantarctic Pacific	37.9	15.9 (19.6)
<b>Indian Ocean</b>	<b>25.5</b>	<b>30.1 (34.3)</b>
Subtropical Indian	15.3	15.3 (17.1)
Tropical Indian	1.3	10.3 (11.4)
Subantarctic Indian	8.9	4.5 (5.8)
<b>Mediterranean Sea</b>	<b>1.1</b>	<b>0.3 (0.4)</b>
<b>Antarctic Marginal Seas</b>	<b>2.1</b>	<b>2.4 (3.3)</b>
Weddell Sea	0.7	0.5 (0.8)
Ross Sea	0.9	0.9 (1.3)
Adélie Region	0.5	1.0 (1.2)

*Note.* The numbers in parenthesis correspond to the regional inventory when the mixed layer is included. Regions in bold represent the sum of the sub-regions listed below. Rounding errors account for the mismatch between the estimates in the text.

the inclusion of oxygen to further constrain the circulation in the TMI could contribute to the differences in  $C_{ant}$  concentration in the equatorial regions. In particular, a deeper ventilation of those regions could be translated to a higher  $C_{ant}$  concentration in the TMI relative to that in OCIM.

Although there are some regional differences among the OCIM and TMI circulation fields, the two matrices are broadly consistent. Carter et al. (2021) compared the surface contributions to a point at the base of the Northern Pacific Subtropical gyre thermocline for the TMI and OCIM in addition to the 2.8° transport matrix from Khatiwala (2007). Despite regional differences, the three matrices show a similar pattern (Figure 1 in Carter et al., 2021). We also note here that the OCIM and the TMI provide similar age estimates for deep and bottom waters (>2,000 m) (DeVries & Primeau, 2011; Gebbie & Huybers, 2012).

### 3. Results

#### 3.1. $C_{ant}$ Injection

The accumulated flux of  $C_{ant}$  across the mixed-layer base in each grid cell from the industrial revolution through 2012 was calculated using Equation 1 (Figure 3). Table 1 summarizes the total injection and inventory in the set of ocean areas defined by Gebbie and Huybers (2010) with additional separation into tropical and subtropical regions at 18° north and south. Of the total ocean inventory of 184.5 Pg C in 2012, 24.3 Pg C remains within the mixed layer, while 160.2 Pg has been injected across the base of the mixed layer. The accumulated injection is largest in deep water formation areas with the strongest flux in the Subpolar North Atlantic (NADW formation region) and Southern Ocean (MIW formation region). Despite its relatively small area (4.2% of the global ocean), the total mass of carbon injected in the Subpolar North Atlantic is 18.2 Pg C (11.3% out of the 160.2 Pg C global total below the mixed layer). 7.1 Pg C (4.4%) of this was injected in the Labrador Sea (including the Irminger Sea and Canadian Archipelago) and 11.1 Pg C (6.9%) in the Nordic Seas. On the other hand, despite being important deep water formation regions with intense fluxes (Figure 3), the Ross and Weddell Seas have contributed with only 1.6 Pg C (1.0%) to the interior ocean inventory.

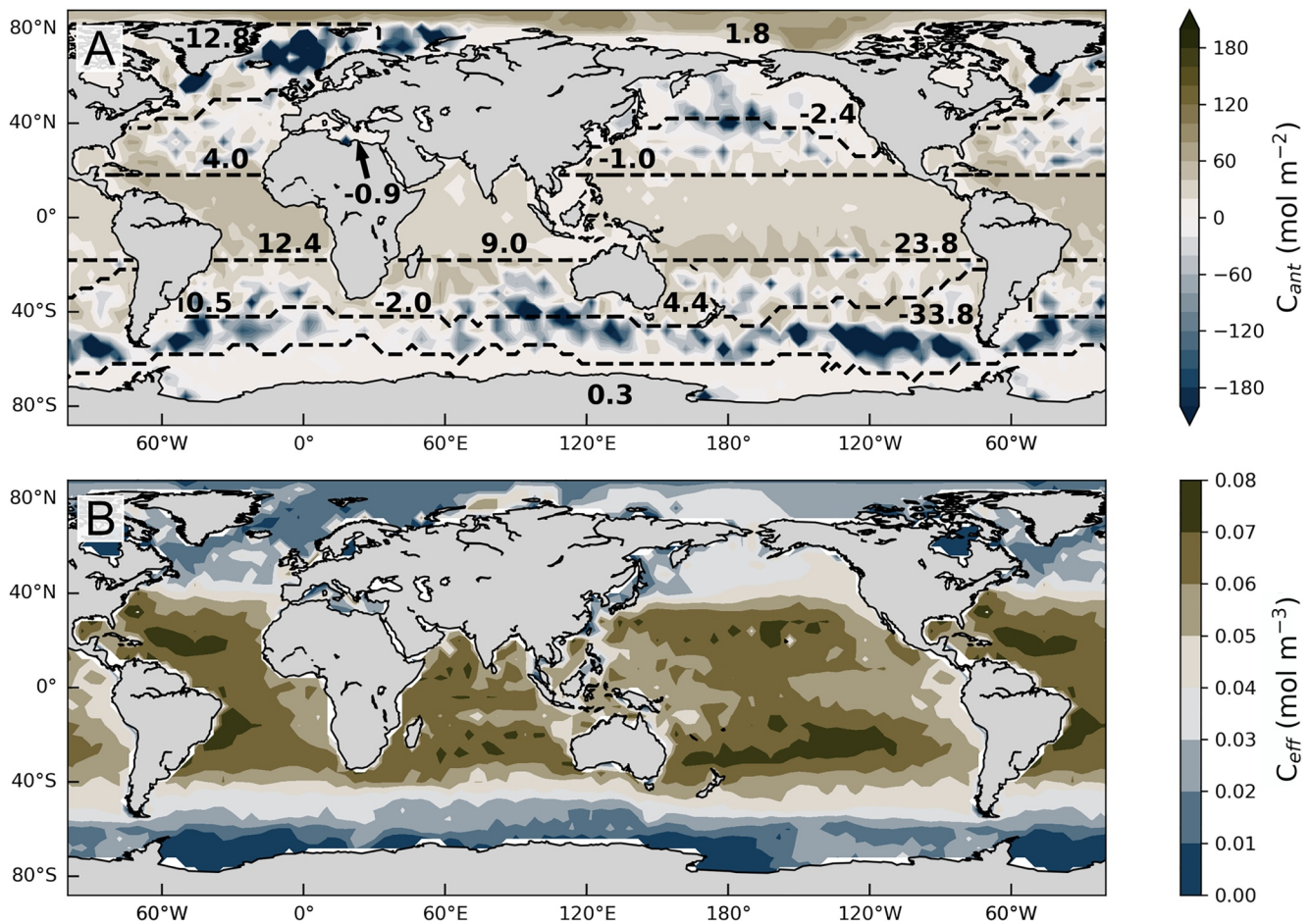


**Figure 4.** (a) The difference between the inventory below the mixed layer and the cumulative fluxes across. Positive values reflect a convergence of  $C_{anti}$ , while negative values reflect a divergence in the ocean interior. The values indicate the net balance of  $C_{anti}$  per region in Pg C. (b) Effective  $C_{anti}$  end-member concentration,  $C_{eff}(s,t)$ , for the waters now residing in the interior ocean, calculated from Equation 3.

The fluxes are also substantial in subtropical regions as a consequence of Subtropical Mode Water (STMW) formation in the subtropical gyres. The fluxes are lowest in tropical regions because of strong stratification and/or upwelling; only 8.6 Pg C (5.4%) has been injected in such regions when summed over the three oceans. Integrated over regions, most of the carbon have been injected in the subtropics (64.3 Pg C or 40.1% of the total injection across the mixed layer) and in the subantarctic region of the Southern Ocean (57.7 Pg C or 36.0%).

The difference between the regional injection and the regional inventory below the mixed layer (Table 1 and Figure 4a) reflects the interior oceanic transport of  $C_{anti}$ . The areas where the amount of injected  $C_{anti}$  is higher than the inventory correspond to regions of  $C_{anti}$  divergence, whereas the areas where the inventory is larger than the injection are regions of  $C_{anti}$  convergence. The Nordic Seas is the region that exports most carbon relative to the injected amount (88.3%). Other areas of strong divergence are the subantarctic region (58.6%), the Labrador Sea (42.3%), as well as the Subpolar North Pacific (38.7%). The  $C_{anti}$  exported from these regions ends up mostly in the tropics, where about one third of the ocean interior  $C_{anti}$  reservoir is found. Here, the  $C_{anti}$  that is imported from other regions is 5.3 times the amount injected locally.

The relative importance of high-latitude deep water formation areas for filling the inner ocean  $C_{anti}$  reservoir has been much smaller than what one would expect from their importance for water volume itself. For instance, while the ratio of water volume injected in the subpolar North Atlantic to the volume injected in the subtropical and tropical Atlantic is approximately 25:3 (Gebbie & Huybers, 2010), the same ratio for  $C_{anti}$  is closer to 1:1 (18.2:20.7, Figure 3). This can be understood when considering that most of the waters from the subtropics and tropics now present in the ocean are much younger and had higher concentrations of  $C_{anti}$  when they were injected



than most of the waters from the high-latitude north Atlantic or Southern Ocean as their resurfacing timescales are much shorter (Primeau & Holzer, 2006). This resurfacing is not explicitly modeled with our approach, but its impacts are included via the age associated with the different water masses. Deep waters from high latitudes remain in the interior ocean on millennial timescales (Primeau & Holzer, 2006) and therefore have higher overall ages. This means they brought with them lower  $C_{ant}$  per volume of water formed compared to water injected in the subtropics and tropics, which have much shorter residence times in the interior ocean as they resurface faster and are overall younger. We illustrate this effect by calculating effective  $C_{ant}$  end-member concentrations:

$$C_{eff}(s, t) = \frac{F(s, t)}{\sum_{\tau=0}^{233} \sum_{i=0}^N g(s, i, \tau)} \quad (3)$$

where the denominator is in effect the total volume of water injected from the mixed-layer patch  $s$  over the industrial era (last 233 years) that has not yet been recycled to the mixed layer, and the numerator is the total mass of  $C_{ant}$  injected as calculated by Equation 1.  $C_{eff}$  is on average 2.3 times higher in the subtropics and subtropics than at high latitudes and up to 4 times higher in individual grid cells (Figure 4b). From the Revelle factor alone, one expects a much smaller concentration gradient and the surface  $C_{ant}$  saturation concentration is only 1.2 times higher in the tropics and subtropics than at high latitudes (Figure S1 in Supporting Information S1). The larger  $C_{ant}$  undersaturation at high latitudes, likely caused by deep mixing that brings low  $C_{ant}$  waters to the surface, increases this to 1.5 (Figure S1 in Supporting Information S1). Thus, most of the regional differences in  $C_{eff}$  are explained by the young ages of waters injected in the tropics and subtropics compared to the high latitudes, which made the injection of  $C_{ant}$  per cubic meter more efficient. The spatial pattern of effective  $C_{ant}$  boundary condition is broadly opposite to the cumulative flux pattern (Figure 3). The largest cumulative fluxes are, however, associated with deep and mode water formation areas, suggesting that the ventilation and mean residence time of the waters in the ocean interior are the rate limiting factor for the ocean carbon uptake.

### 3.2. Deep Injection

Ocean-based Carbon Dioxide Removal strategies, such as injection of  $\text{CO}_2$  in the ocean by various means, have been proposed to achieve negative emissions, and 1,000 m has been previously used as an approximation for the depth at which  $C_{ant}$  can be sequestered for centennial timescales (Passow & Carlson, 2012), and while this is approximately correct, the actual sequestration timescale varies regionally (Primeau, 2005; Siegel et al., 2021). Here, we therefore set a uniform boundary at 1,000 m to separate the intermediate ocean reservoirs of  $C_{ant}$  of 142.2 Pg C (77.1%) and the deep reservoir of 42.3 Pg C (22.9%) for 2012. Our results provide broad insight into which surface regions contribute to the  $C_{ant}$  stored below 1,000 m and therefore, a large part of the  $C_{ant}$  stored for approximately centennial timescales.

Not every region has the same role in filling the deep ocean. By modifying the selection of interior points  $i$  in Equation 1, we can determine where  $C_{ant}$  stored in any particular part of the global ocean was subducted out of the mixed layer (Figure 5). The largest of such fluxes are found in the Subpolar North Atlantic, where altogether 14.9 Pg C has been injected deeper than 1,000 m, as associated with the formation of NADW. This is 81.9% of the  $C_{ant}$  injected across the mixed-layer base in this region, meaning that most of the carbon injected there end up at more than 1,000 m depth. The subantarctic region is the other main injection region where, by the formation of MIW, 19.4 Pg C are injected (45.9% of the total injection to levels deeper than 1,000 m). The STMW in the subtropical gyres contributes to only 6.2 Pg C to the deep ocean, a much smaller fraction (14.7%) of the total injection below 1,000 m. In the Mediterranean Sea, 0.8 Pg C are injected below 1,000 m, almost three quarters of the total  $C_{ant}$  injected in this region, by means of the Mediterranean Overflow waters that enter the North Atlantic at  $\sim$ 1,000 m depth (Aldama-Campino & DÖös, 2020).

The  $C_{ant}$  stored in the deep Atlantic and Arctic (Atlantic-Arctic), Pacific, Indian, and Southern oceans mostly originates from high latitudes (Figures 6b–6e). The deep Atlantic (Figure 6b) has accumulated 18.1 Pg C, and most of it was injected in the Nordic Seas (8.5 Pg C) and the Labrador Sea (4.5 Pg C). The deep Pacific (Figure 6c) stores 12.3 Pg  $C_{ant}$ , and a large part (8.2 Pg C) was injected in the subantarctic region with the MIW formed there. Some (0.6 Pg C) has also been injected in the North Pacific with the formation of North Pacific Intermediate Water. In addition, both the Subpolar North Atlantic and the Arctic contribute to the deep Pacific  $C_{ant}$  inventory (0.3 and 0.2 Pg C). The deep Indian (Figure 6d) ocean  $C_{ant}$  reservoir has been filled similarly. It stores 4.5 Pg C

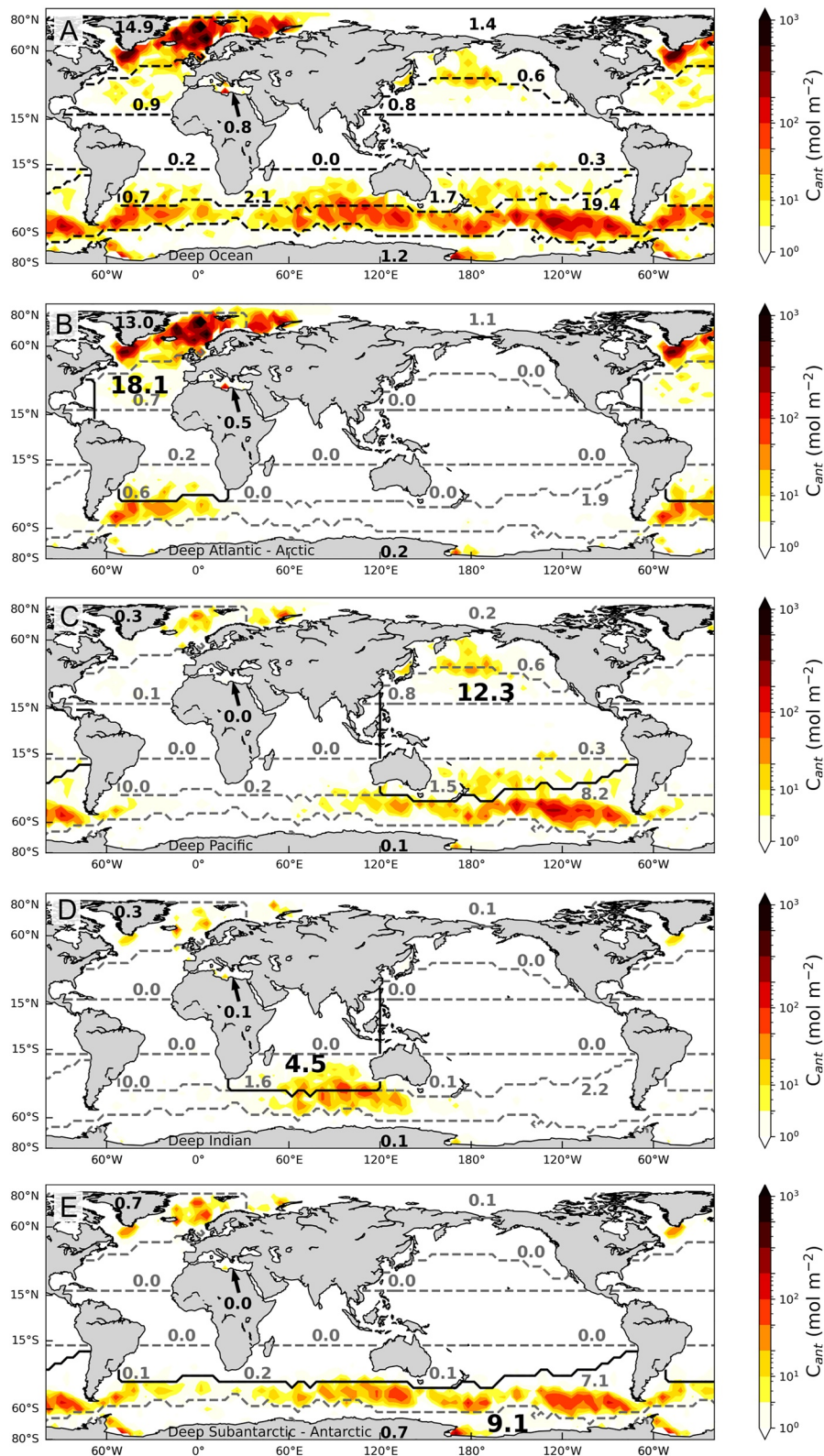


**Figure 5.** Same as Figure 3 but for (a)  $C_{ant}$  fluxes into the deep ocean (>1,000 m) and (b–e) the deep reservoirs of major oceanic regions. For (b–e): The solid black line marks the horizontal limit of the respective deep reservoir and the number in black indicates the total mass of  $C_{ant}$  stored within the reservoir in Pg C. Colors show the fluxes across the mixed layer, where gray-dashed lines delimit the surface injection regions and gray numbers give the total mass of  $C_{ant}$  injected within each of these regions (in Pg C). The color scales are logarithmic. Numbers for total mass are consistent with each other within rounding errors.

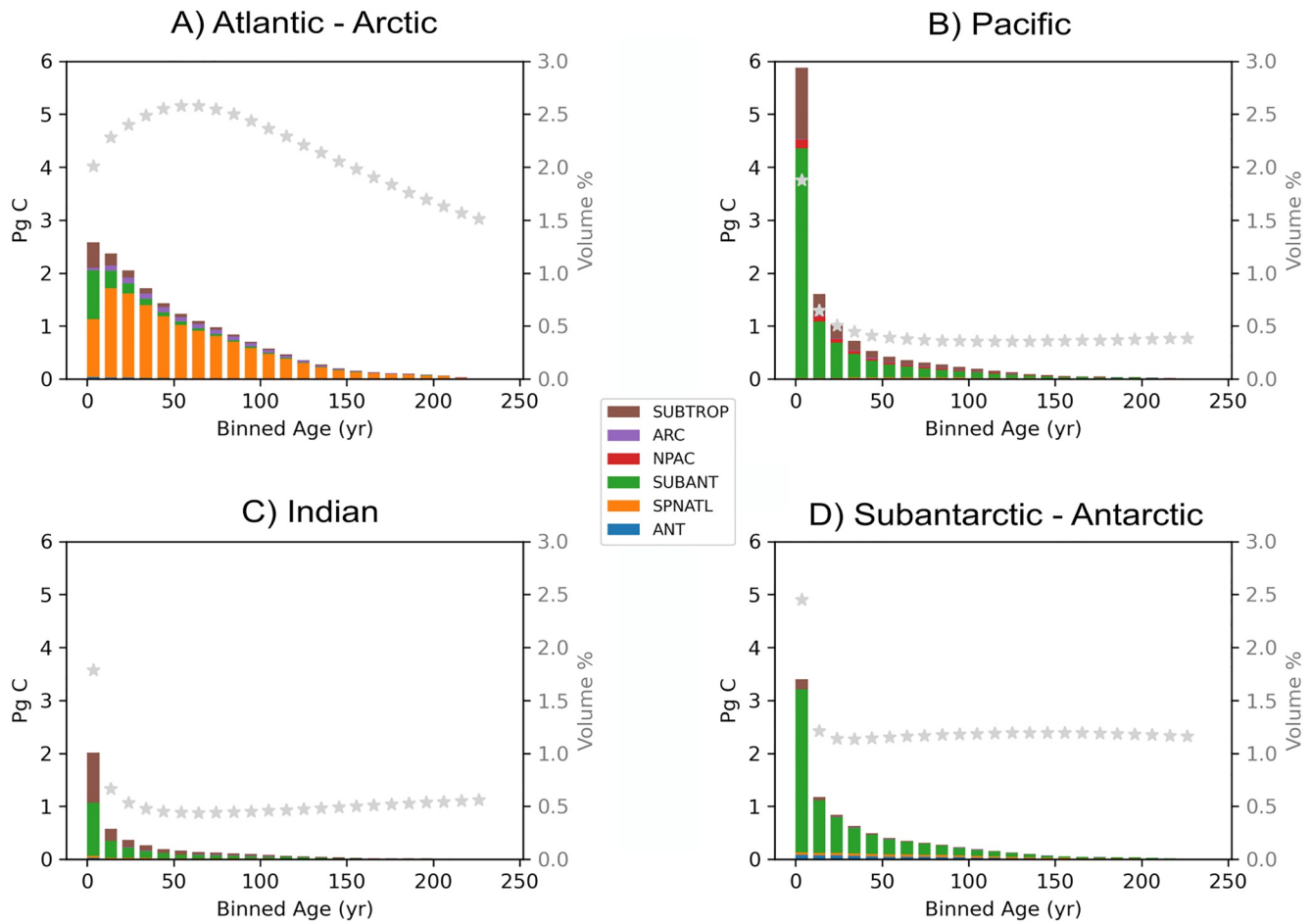


**Figure 6.** Age distribution of  $C_{anti}$  below 1,000 m for 2012 in the major ocean regions considered here, showing where and when the  $C_{anti}$  stored in the deep (a) Atlantic (including the Arctic), (b) Pacific, (c) Indian, and (d) Antarctic was injected across the mixed layer. The different colors refer to the region of injection: ANT (Antarctic), SPNATL (Subpolar North Atlantic), SUBANT (Subantarctic), NPAC (North Pacific), and ARC (Arctic). Gray stars indicate the water-age distribution as volume percentage of the entire reservoir for each age class for the last 233 years. The age distribution was binned every 10 years.

of which a third (1.6 Pg C) was injected locally but the main fraction has been transported from the subantarctic region through the subduction with MIW (2.2 Pg C). The Subpolar North Atlantic also contributes to the deep Indian Ocean  $C_{anti}$  reservoir (0.3 Pg C). The deep Subantarctic-Antarctic (Figure 6e) stores 9.1 Pg C of which most (7.1 Pg C) were injected north of the Polar Front by the MIW. Antarctic Bottom Water (AABW) from the Ross and Weddell Seas have relatively minor contributions to the deep  $C_{anti}$  stored in this reservoir, 0.4 and 0.3 Pg C, respectively. The Subpolar North Atlantic contributes also with 0.7 Pg C through the southward transport of NADW. Overall, these results highlight how the deep, long-term,  $C_{anti}$  storage in the ocean relies on a few key regions.

For each of the pathways that connect a subduction region to a long-term reservoir, there is an associated water-age distribution, which is equivalent to the boundary Green's function. How long it takes for each of the deep reservoirs to be filled is, essentially, the age distribution of  $C_{anti}$  below 1,000 m in the oceanic region in question (Figure 6). This distribution results from the convolution of the water-age distribution and the  $C_{anti}$  concentration at the time of subduction (i.e., the boundary condition). The  $C_{anti}$ -age distribution is calculated by removing the temporal summation in Equation 1 and selecting the interior points  $i$  within the deep reservoir  $R$ :

$$F(t, \tau) = \sum_{s=0}^{2806} \sum_{i=0}^N g(s, i, \tau) c(s, t - \tau) \quad \text{where } i \in R. \quad (4)$$

The  $C_{ant}$ -age distributions (Figures 6a–6d) show that young  $C_{ant}$  predominates in all deep reservoirs. The lower amount of  $C_{ant}$  at the tail end of the distribution reflects the smaller  $C_{ant}$  concentration in waters ventilated at the beginning of the industrial era. In the deep Atlantic-Arctic, the  $C_{ant}$  is older than in the rest of the deep reservoirs. This is a consequence of the presence of large fractions of water at older ages in the Atlantic-Arctic region; about 50% of the reservoir has been ventilated during the industrial period up to  $\sim 2.5\%$  for each 10-year interval shown (Figure 6a). Such large ventilated water volume, combined with the appreciable amount of  $C_{ant}$  present in the atmosphere at the time they were ventilated, leads to quite high concentrations of  $C_{ant}$  (not shown). Even if the volume fraction of waters at ages 40 to  $\sim 100$  years is large, these waters contribute less to the  $C_{ant}$  inventory because of their smaller  $C_{ant}$  concentrations. In the deep Pacific, Indian, and Subantarctic-Antarctic oceans, waters ventilated in the industrial era constitute only a small part of the total volume (10.6%, 12.9%, and 28.7%, respectively) (see longer age spectra in Figure S2 in Supporting Information S1). The volume fraction of waters younger than 10 years is relatively large, likely resulting from the vigorous ventilation of the MIW. The combination of large volume fraction and high  $C_{ant}$  concentrations in these recent waters results in a strong peak of  $C_{ant}$  for the 10-year age class. For the rest of the industrial period, the various age classes in the Pacific and Indian contribute quite equally to volume, about 0.5% for each 10-year interval. Counterintuitively, the smaller amount of  $C_{ant}$  present in the deep Pacific and Indian oceans is thus younger than the large amounts present in the deep Atlantic-Arctic. In the Pacific and Indian oceans,  $C_{ant}$  has entered primarily from ventilation of the thermocline in the subtropics (SUBTROP contribution in Figure 6) and with MIW from the subantarctic (SUBANT).

## 4. Discussion

### 4.1. Comparison With Other Estimates

The  $C_{ant}$  injection calculated here represents the cumulative fluxes across the mixed-layer base and is comparable to the annual fluxes determined by Bopp et al. (2015). Their modeling approach and the observationally derived Green's function approach presented here provide consistent results. Overall, the studies agree that substantial amounts of  $C_{ant}$  are injected in the subtropical gyres and in the Southern Ocean, while they disagree in the Subpolar North Atlantic. In both studies, the subtropics inject the highest amount of  $C_{ant}$ . The injection across the mixed-layer base in the Southern Ocean as derived from the Green's function is 31.3% (57.7 Pg C) of the total ocean inventory of 184.5 Pg C, whereas in Bopp et al. (2015), 0.74 Pg C yr<sup>-1</sup> are injected, corresponding to 32.5% of their annual mean global uptake over 1998–2007. The injection north of 49°N is, in our case, substantially higher than the 5.7% of the yearly uptake from Bopp et al. (2015) at 14.3% (26.4 Pg C) of the total inventory, and the difference is mainly associated with the Labrador and Nordic Seas.

Bopp et al. (2015) pointed out that their modeled inventory in the North Atlantic was slightly underestimated and therefore, it is possible that the vertical transports were also underestimated. Some models struggle to represent the small-scale processes involved in deep water formation in the Subpolar North Atlantic (Heuzé, 2017, 2021), such that weak mixing and ventilation results in a lower  $C_{ant}$  uptake (Wang et al., 2012). The NEMO-PISCES model used by Bopp et al. (2015) is based on the OPA ocean circulation model (Madec, 2008) and the LIM2 ice model (Timmerman et al., 2005). These are shared by the ocean/sea-ice model used at NOCS (National Oceanography Centre Southampton), which showed one of the shallowest March mean mixed-layer depths among the models compared by Danabasoglu et al. (2014). Shallower mixed-layer depths were correlated with a weak Atlantic Meridional Overturning Circulation (AMOC) (Danabasoglu et al., 2014), which translates into smaller transport of  $C_{ant}$  to depths below 1,000 m (Goris et al., 2018). Furthermore, the NEMO-PISCES model has been shown to misrepresent the Nordic Seas Overflow and underestimate its  $C_{ant}$  transport (Racapé et al., 2018). In general, there is an ongoing discussion on how accurately the models represent the deep water formation in the North Atlantic (Menary et al., 2020) and thus the  $C_{ant}$  transports. Our approach, based on the TMI model, provides a validation data set by empirically fitting modern observations. As a result, the TMI better captures the higher  $C_{ant}$  concentrations in NADW compared to some coarse-resolution models; yet, these are lower than in other observation-based models (DeVries, 2014; Gruber et al., 2019).

Our results suggest that the downward transports of  $C_{ant}$  in the Nordic Seas are 1.6 times larger than in the Labrador Sea (Table 1). Such a dominant role of the Nordic Seas agrees with recent observations of the contribution of these regions to the lower limb of the AMOC across the OSNAP (Overturning in the Subpolar North Atlantic Program) current meter array located in the Subpolar North Atlantic and presented by Lozier et al. (2019). Specifically, they found that the contribution from the Labrador Sea (through the OSNAP-West array) to the overturning

circulation ( $2.1 \pm 0.3$  Sv) was substantially smaller than the contribution from the Nordic Seas, Irminger Sea, and Iceland basin ( $15.6 \pm 0.8$  Sv through the OSNAP-East array) over late 2014 through spring 2016. For a more specific comparison, we estimated the subduction rates of volume north of OSNAP-West and north of OSNAP-East by integrating volume contributions from the Green's function over time as in Primeau and Holzer (2006). Our calculated subduction rates of 2.6 Sv north of OSNAP-West and 12.6 Sv north of OSNAP-East agree well with the direct current measurements presented by Lozier et al. (2019). This renders confidence to our results and further suggests that a dominance of northeastern sources to the lower limb is a persistent feature of the AMOC as the TMI analyses were conducted using climatological data and the assumption of a statistical steady state. We further determined the contribution from the Nordic Seas across the Greenland-Scotland Ridge to 8.1 Sv in the Green's function, which is in excellent agreement with the transport estimate by Østerhus et al. (2019) of  $7.8 \pm 1.9$  Sv and by Chafik and Rossby (2019) of 6.87 Sv. A more direct evaluation of our estimated  $C_{ant}$  export from the Nordic Seas is possible by comparing to the  $C_{ant}$  budget from Jeansson et al. (2011). They reported that  $0.09 \text{ Pg C yr}^{-1}$  of  $C_{ant}$  were transported southward by the overflow waters across the Greenland-Scotland Ridge in 2002. This transport represents 4.5% of the global air-sea  $\text{CO}_2$  flux for 2002, which agrees extremely well with the 4.2% ( $7.8 \text{ Pg C}$ ) export relative to the global  $C_{ant}$  inventory found in our study.

Our results show that the Southern Ocean has injected 31.3% of the total inventory of  $C_{ant}$  across the mixed layer, consistent with its widely recognized key role for the downward transports of  $C_{ant}$ . In comparison, Sallée et al. (2012) suggested in their observation-based regional study that these fluxes are about 20% (south of  $35^\circ\text{S}$ ) of the global annual air-sea  $C_{ant}$  flux of  $2.0 \pm 0.6 \text{ Pg C}$  (Friedlingstein et al., 2020). One can also consider the regional air-sea flux of  $C_{ant}$  as the upper limit for the injection across the mixed layer in the Southern Ocean, given the limited advection of  $C_{ant}$  with surface waters into this region. Several studies agree that the Southern Ocean  $C_{ant}$  uptake corresponds to 30%–40% of the global uptake (DeVries, 2014; Frölicher et al., 2015; Gruber et al., 2018; Khatiwala et al., 2013; Mikaloff-Fletcher et al., 2006; Sallée et al., 2012). Because of the large volumes of MIW and AABW water that is formed, one can expect that most of the transport in the Southern Ocean occur below the mixed layer and therefore the injection estimates do not fall far from the uptake. Thus, our estimate (31.3%) falls between the upper limit determined by the air-sea  $C_{ant}$  fluxes and the observed 20% (Sallée et al., 2012). We finally note that our estimate is fully consistent with the 32.5% modeled by Bopp et al. (2015).

The agreement with other estimates strengthens our confidence in the results and we believe that the differences in the ocean circulation between the TMI and OCIM, which result in differences in total inventory (Figure 1d), have a small impact on the general pattern of the fluxes through the mixed layer. In the North Atlantic, differences resulting from circulation (Section 2.3) suggest that the injection estimates as derived from the Green's function are lower in the Subpolar North Atlantic than in the OCIM. Similarly, the positive differences in the equatorial thermocline suggest a slightly higher injection in the subtropics in the Green's function estimates. Another aspect to bear in mind is that the ocean circulation and biogeochemistry are considered steady state (i.e., time invariant), which is a common assumption in transport matrices. Model simulations show that the global impact of these assumptions is small. Changes in circulation lead to an uncertainty in the total inventory of less than 1% or 4% when also accounting for variations in biogeochemistry (Wang et al., 2012). Regionally, however, errors in  $C_{ant}$  estimates derived from steady-state transport matrices associated with lack of representation of circulation changes are of the same order of magnitude as errors in data-based estimates (Khatiwala et al., 2013). Recent observational studies indicate that decadal changes in circulation do occur and that this affects both the transport and distribution of  $C_{ant}$  (DeVries et al., 2017; Gruber et al., 2019), which would impact both the pattern and intensity of  $C_{ant}$  injection. Therefore, the results presented in this study should be considered and interpreted in a climatological sense.

#### 4.2. Climate Sensitivity Timescales

Because each of the pathways that connect a subduction region to a long-term reservoir has an associated transit time (Figure 6), we are able to infer where and over what timescales a change in surface anthropogenic carbon uptake will be detectable in the deep ( $>1,000$  m) reservoirs. We refer to this as climate sensitivity timescales. The transit times vary spatially; thus, the climate sensitivity timescales are specific to each of the injection regions. For example, under current atmospheric  $\text{CO}_2$  growth rates, the response in  $C_{ant}$  storage for a change in the surface forcing in the Subpolar North Atlantic will be strongest after 20 years in the Atlantic-Arctic reservoir (Orange bars in Figure 6a), but the signal would be weakened and lost by the time it reaches the rest of the reservoirs as a

consequence of extensive diffusion along the way (Primeau, 2005). On the other hand, a change in the forcing in the subantarctic region would strongly impact the  $C_{ant}$  storage in the deep Pacific, Indian, and Subantarctic-Arctic reservoirs within a decade, given that the  $C_{ant}$ -age distribution is biased young and the small size of the inventory there. We note, however, that the relative importance of the short-term signal might decrease as these reservoirs fill. The region contaminated with  $C_{ant}$ , or ventilated during the industrial era, amounts to a very small fraction of the entire reservoirs (Figure 6) as the waters deeper than 1,000 m in North Pacific are mostly ventilated by the AABW at millennial timescales (Holzer et al., 2021).

## 5. Summary

The TMI and its derived Green's function, built using observations of ocean tracers, have allowed us to investigate how the ocean anthropogenic carbon reservoir has been filled. By following the mixing pathways that connect any ocean interior point with the surface, we determined where and when  $C_{ant}$  was injected across the mixed-layer base and into the interior ocean from the beginning of the industrial era through 2012.

Most of the  $C_{ant}$  currently stored in the ocean interior were injected in high-latitude mode and deep water formation regions and in the subtropics. The Southern Ocean is the main injection region, where about one third of the  $C_{ant}$  stored in the interior ocean crossed the mixed layer carried by the MIW (Mode and Intermediate Waters: SAMW and AAIW). Other important injection regions are the subtropics through the STMW formation and the Subpolar North Atlantic by means of NADW formation. Most of the  $C_{ant}$  injected in these regions are transported away, mostly into the tropics where the reservoir size is five times larger than the amount of  $C_{ant}$  injected locally. Here, we highlight the Nordic Seas, where very little of the injected  $C_{ant}$  remains in the region. At the same time, the Subpolar North Atlantic has been one of the most inefficient regions in terms of  $C_{ant}$  injected per unit volume, a pattern shown to be common for high latitudes and related to the low buffer capacity of these waters, the rapid ventilation of surface waters by vigorous mixing, and the longer residence time of these waters in the interior ocean. On the contrary, subtropical regions have been the most efficient injecting  $C_{ant}$  per unit of volume.

At least one fifth of the total  $C_{ant}$  injected since preindustrial times has now reached depths greater than 1,000 m, which constitutes the deep, long-term reservoir where most of the  $C_{ant}$  are stored for centennial timescales. Although the deep injection pattern is similar to the total injection, the relative importance of each of the regions differs. A relatively small proportion of the  $C_{ant}$  injected in the subtropics ends up in the deep ocean, while this proportion is much higher in the Southern Ocean and the Nordic Seas, which are the most important regions in transporting  $C_{ant}$  into the deep ocean.

The source region and timescale at which the deep reservoir is filled vary regionally. The deep Pacific, Indian, and Subantarctic-Arctic reservoirs have been only recently filled with  $C_{ant}$  subducted in the Southern Ocean, and the age of the  $C_{ant}$  is therefore young. The  $C_{ant}$  in the deep Atlantic-Arctic and Antarctic is older due to the shorter transit times, which allowed those regions to be filled at earlier times.

Future work is needed to constrain the fluxes of  $C_{ant}$  from tracers. The TMI offers the advantage of being derived mostly from observations; however, the ventilation rates are dependent on the  $^{14}\text{C}$  observations, which are sparse in many regions (e.g., the Arctic). New  $^{14}\text{C}$  measurements in combination with other ocean tracers, such as CFCs and SF6 gases, would provide a better constraint on the ventilation rates in the TMI and similar methods.

## Data Availability Statement

The Total Matrix Intercomparison transport matrix used in this study to produce the anthropogenic carbon fields as well as the Green's functions is published by Gebbie & Huybers (2012) and is available in GitHub (<https://github.com/ggebbie/TMI.mat>). The anthropogenic carbon boundary condition is published by DeVries (2014) and GLODAP mapped climatology by Lauvset et al. (2016).

## References

- Aldama-Campino, A., & DÖös, K. (2020). Mediterranean overflow water in the North Atlantic and its multidecadal variability. *Tellus, Series A: Dynamic Meteorology and Oceanography*, 72(1), 1–10. <https://doi.org/10.1080/16000870.2018.1565027>
- Álvarez, M., Ríos, A. F., Pérez, F. F., Bryden, H. L., & Rosón, G. (2003). Transports and budgets of total inorganic carbon in the subpolar and temperate North Atlantic. *Global Biogeochemical Cycles*, 17(1), 2–1. <https://doi.org/10.1029/2002gb001881>

### Acknowledgments

We thank Tim DeVries and an anonymous reviewer for their constructive reviews. X. Davila was supported by a PhD research fellowship from the University of Bergen. G. Gebbie was supported by U.S. NSF Grant 88075300. A. Brakstad was supported by the Trond Mohn Foundation under grant agreement BFS2016REK01. E. L. McDonagh was supported by UKRI grants Atlantic Biogeochemical fluxes (ref no. NE/M005046/2) and TICTOC: Transient tracer-based Investigation of Circulation and Thermal Ocean Change (ref no. NE/P019293/2). A. Olsen and S. K. Lauvset appreciate support from the Research Council of Norway (ICOS-Norway, project number 245972). J. Schwinger acknowledges support by the Research Council of Norway through project INES (project number 270061). Supercomputer time and storage resources were provided by the The Norwegian e-infrastructure for Research Education (UNINETT Sigma2, projects nn2980k and ns2980k).

- Anderson, L. A., & Sarmiento, J. L. (1994). Redfield ratios of remineralization determined by nutrient data analysis. *Global Biogeochemical Cycles*, 8(1), 65–80. <https://doi.org/10.1029/93GB03318>
- Aumont, O., & Bopp, L. (2006). Globalizing results from ocean in situ iron fertilization studies. *Global Biogeochemical Cycles*, 20(2). <https://doi.org/10.1029/2005GB002591>
- Bopp, L., Lévy, M., Resplandy, L., & Sallée, J. B. (2015). Pathways of anthropogenic carbon subduction in the global ocean. *Geophysical Research Letters*, 42(15), 6416–6423. <https://doi.org/10.1002/2015GL065073>
- Carter, B. R., Feely, R. A., Lauvset, S. K., Olsen, A., DeVries, T., & Sonnerup, R. (2021). Preformed properties for marine organic matter and carbonate mineral cycling quantification. *Global Biogeochemical Cycles*, 35(1), e2020GB006623. <https://doi.org/10.1029/2020GB006623>
- Chafik, L., & Rossby, T. (2019). Volume, heat, and freshwater Divergences in the subpolar North Atlantic suggest the Nordic Seas as key to the state of the meridional overturning circulation. *Geophysical Research Letters*, 46(9), 4799–4808. <https://doi.org/10.1029/2019GL082110>
- Danabasoglu, G., Yeager, S. G., Bailey, D., Behrens, E., Bentsen, M., Bi, D., et al. (2014). North Atlantic simulations in coordinated ocean-ice reference experiments phase II (CORE-II). Part I: Mean states. *Ocean Modelling*, 73, 76–107. <https://doi.org/10.1016/j.ocemod.2013.10.005>
- DeVries, T. (2014). The oceanic anthropogenic CO<sub>2</sub> sink: Storage, air-sea fluxes, and transports over the industrial era. *Global Biogeochemical Cycles*, 1–17. <https://doi.org/10.1002/2013GB004739>
- DeVries, T., Holzer, M., & Primeau, F. (2017). Recent increase in oceanic carbon uptake driven by weaker upper-ocean overturning. *Nature*, 542(7640), 215–218. <https://doi.org/10.1038/nature21068>
- DeVries, T., & Primeau, F. (2011). Dynamically and observationally constrained estimates of water-mass distributions and ages in the global ocean. *Journal of Physical Oceanography*, 41(12), 2381–2401. <https://doi.org/10.1175/JPO-D-10-05011.1>
- England, M. H., & Maier-Reimer, E. (2001). Using chemical tracers to assess ocean models. *Reviews of Geophysics*, 39(1), 29–70. <https://doi.org/10.1029/1998RG000043>
- Friedlingstein, P., O'Sullivan, M., Jones, M. W., Andrew, R. M., Hauck, J., Olsen, A., et al. (2020). Global carbon budget 2020. *Earth System Science Data*, 12(4), 3269–3340. <https://doi.org/10.5194/essd-12-3269-2020>
- Frölicher, T. L., Sarmiento, J. L., Paynter, D. J., Dunne, J. P., Krasting, J. P., & Winton, M. (2015). Dominance of the Southern Ocean in anthropogenic carbon and heat uptake in CMIP5 models. *Journal of Climate*, 28(2), 862–886. <https://doi.org/10.1175/JCLI-D-14-00117.1>
- Gebbie, G. (2012). Tracer transport timescales and the observed Atlantic-Pacific lag in the timing of the Last Termination. *Paleoceanography*, 27(3), 1–14. <https://doi.org/10.1029/2011PA002273>
- Gebbie, G., & Huybers, P. (2010). Total matrix Intercomparison: A method for determining the geometry of water-mass pathways. *Journal of Physical Oceanography*, 40(8), 1710–1728. <https://doi.org/10.1175/2010jpo4272.1>
- Gebbie, G., & Huybers, P. (2012). The mean age of ocean waters inferred from radiocarbon observations: Sensitivity to surface sources and accounting for mixing histories. *Journal of Physical Oceanography*, 42(2), 291–305. <https://doi.org/10.1175/jpo-d-11-043.1>
- Goris, N., Tjiputra, J. F., Olsen, A., Schwinger, J., Lauvset, S. K., & Jeansson, E. (2018). Constraining projection-based estimates of the future North Atlantic carbon uptake. *Journal of Climate*, 31(10), 3959–3978. <https://doi.org/10.1175/JCLI-D-17-0564.1>
- Graven, H. D., Gruber, N., Key, R., Khatiwala, S., & Giraud, X. (2012). Changing controls on oceanic radiocarbon: New insights on shallow-to-deep ocean exchange and anthropogenic CO<sub>2</sub> uptake. *Journal of Geophysical Research*, 117(10), 1–16. <https://doi.org/10.1029/2012JC008074>
- Gruber, N., Clement, D., Carter, B. R., Feely, R. A., Heuven, S. V., Hoppema, M., et al. (2019). The oceanic sink for anthropogenic CO<sub>2</sub> from 1994 to 2007. *Science*, 363(6432), 1193–1199. <https://doi.org/10.1126/science.aau5153>
- Gruber, N., Landschützer, P., & Lovenduski, N. S. (2018). The variable Southern Ocean carbon sink. *Annual Review of Marine Science*, 9(1), 159–186. <https://doi.org/10.1146/annurev-marine-121916-063407>
- Heuzé, C. (2017). North Atlantic deep water formation and AMOC in CMIP5 models. *Ocean Science Discussions*, 1–22. <https://doi.org/10.5194/os-2017-2>
- Heuzé, C. (2021). Antarctic bottom water and North Atlantic deep water in CMIP6 models. *Ocean Science*, 17(1), 59–90. <https://doi.org/10.5194/os-17-59-2021>
- Holfort, J., Johnson, K. M., Schneider, B., Siedler, G., & Wallace, D. W. (1998). Meridional transport of dissolved inorganic carbon in the South Atlantic Ocean. *Global Biogeochemical Cycles*, 12(3), 479–499. <https://doi.org/10.1029/98GB01533>
- Holzer, M., DeVries, T., & de Lavergne, C. (2021). Diffusion controls the ventilation of a Pacific Shadow Zone above abyssal overturning. *Nature Communications*, 1–13, 4348. <https://doi.org/10.1038/s41467-021-24648-x>
- Iudicone, D., Rodgers, K. B., Plancherel, Y., Aumont, O., Ito, T., Key, R. M., et al. (2016). The formation of the ocean's anthropogenic carbon reservoir. *Scientific Reports*, 6(1), 1–16. <https://doi.org/10.1038/srep35473>
- Jeansson, E., Olsen, A., Eldevik, T., Skjelvan, I., Omar, A. M., Lauvset, S. K., et al. (2011). The Nordic Seas carbon budget: Sources, sinks, and uncertainties. *Global Biogeochemical Cycles*, 25(4), 1–16. <https://doi.org/10.1029/2010GB003961>
- Khatiwala, S. (2007). A computational framework for simulation of biogeochemical tracers in the ocean. *Global Biogeochemical Cycles*, 21(3), 1–14. <https://doi.org/10.1029/2007GB002923>
- Khatiwala, S., Primeau, F., & Hall, T. (2009). Reconstruction of the history of anthropogenic CO<sub>2</sub> concentrations in the ocean. *Nature*, 462(7271), 346–349. <https://doi.org/10.1038/nature08526>
- Khatiwala, S., Tanhua, T., Mikaloff Fletcher, S., Gerber, M., Doney, S. C., Graven, H. D., et al. (2013). Global ocean storage of anthropogenic carbon. *Biogeosciences*, 10(4), 2169–2191. <https://doi.org/10.5194/bg-10-2169-2013>
- Lauvset, S. K., Carter, B. R., Perez, F. F., Jiang, L. Q., Feely, R. A., Velo, A., & Olsen, A. (2020). Processes driving global interior ocean pH distribution. *Global Biogeochemical Cycles*, 34(1), 1–17. <https://doi.org/10.1029/2019GB006229>
- Lauvset, S. K., Key, R. M., Olsen, A., Van Heuven, S., Velo, A., Lin, X., et al. (2016). A new global interior ocean mapped climatology: The 1° × 1° GLODAP version 2. *Earth System Science Data*, 8(2), 325–340. <https://doi.org/10.5194/essd-8-325-2016>
- Liddicoat, S. K., Wiltshire, A. J., Jones, C. D., Arora, V. K., Brovkin, V., Cadule, P., et al. (2021). Compatible fossil fuel CO<sub>2</sub> emissions in the CMIP6 Earth System models' historical and shared socioeconomic pathway experiments of the twenty-first century. *Journal of Climate*, 34(8), 2853–2875. <https://doi.org/10.1175/JCLI-D-19-0991.1>
- Lozier, M. S., Li, F., Bacon, S., Bahr, F., Bower, A. S., Cunningham, S. A., et al. (2019). A sea change in our view of overturning in the subpolar North Atlantic. *Science*, 363(6426), 516–521. <https://doi.org/10.1126/science.aau6592>
- Lundberg, L., & Haugan, P. M. (1996). A Nordic Seas-Arctic Ocean carbon budget from volume flows and inorganic carbon data. *Global Biogeochemical Cycles*, 10(3), 493–510. <https://doi.org/10.1029/96GB00359>
- Macdonald, A. M., Baringer, M. O., Wanninkhof, R., Lee, K., & Wallace, D. W. (2003). A 1998–1992 comparison of inorganic carbon and its transport across 24.5°N in the Atlantic. *Deep-Sea Research Part II Topical Studies in Oceanography*, 50(22–26), 3041–3064. <https://doi.org/10.1016/j.dsr2.2003.07.009>
- Madec, G. (2008). *NEMO Ocean Engine* (Vol. 27). Institut Pierre-Simon Laplace (IPSL). <https://doi.org/10.5281/zenodo.3878122>

- Madec, G., Delecluse, P., Imbard, M., & Lévy, C. (1998). *OPA 8.1 ocean general circulation model reference manual* (Vol. 11, p. 91). Note du Pole de modélisation, Institut Pierre-Simon Laplace (IPSL).
- Maier-Reimer, E., & Hasselmann, K. (1987). Transport and storage of CO<sub>2</sub> in the ocean. *Climate Dynamics*, 2(2), 63–90. <https://doi.org/10.1007/BF01054491>
- McNeil, B. I., Matear, R. J., Key, R. M., Bullister, J. L., & Sarmiento, J. L. (2003). Anthropogenic CO<sub>2</sub> uptake by the ocean based on the global chlorofluorocarbon data set. *Science*, 299(5604), 235–239. <https://doi.org/10.1126/science.1077429>
- Menary, M. B., Jackson, L. C., & Lozier, M. S. (2020). Reconciling the relationship between the AMOC and Labrador Sea in OSNAP observations and climate models. *Geophysical Research Letters*, 47(18). <https://doi.org/10.1029/2020GL089793>
- Middelburg, J. J., Soetaert, K., & Hagens, M. (2020). Ocean alkalinity, buffering and biogeochemical processes. *Reviews of Geophysics*, 58(3). <https://doi.org/10.1029/2019RG000681>
- Mikaloff-Fletcher, S. E., Gruber, N., Jacobson, A. R., Doney, S. C., Dutkiewicz, S., Gerber, M., et al. (2006). Inverse estimates of anthropogenic CO<sub>2</sub> uptake, transport, and storage by the ocean. *Global Biogeochemical Cycles*, 20(2), 1–16. <https://doi.org/10.1029/2005GB002530>
- Olsen, A., Omar, A. M., Jeansson, E., Anderson, L. G., & Bellerby, R. G. (2010). Nordic seas transit time distributions and anthropogenic CO<sub>2</sub>. *Journal of Geophysical Research*, 115(5), 1–14. <https://doi.org/10.1029/2009JC005488>
- Østerhus, S., Woodgate, R., Valdimarsson, H., Turrell, B., de Steur, L., Quadfasel, D., et al. (2019). Arctic Mediterranean exchanges: A consistent volume budget and trends in transports from two decades of observations. *Ocean Science Discussions*, 1–37. <https://doi.org/10.5194/os-2018-114>
- Passow, U., & Carlson, C. A. (2012). The biological pump in a high CO<sub>2</sub> world. *Marine Ecology Progress Series*, 470(2), 249–271. <https://doi.org/10.3354/meps09985>
- Primeau, F. W. (2005). Characterizing transport between the surface mixed layer and the ocean interior with a forward and adjoint global ocean transport model. *Journal of Physical Oceanography*, 35(4), 545–564. <https://doi.org/10.1175/JPO2699.1>
- Primeau, F. W., & Holzer, M. (2006). The Ocean's memory of the atmosphere: Residence-time and ventilation-rate distributions of water masses. *Journal of Physical Oceanography*, 36(7), 1439–1456. <https://doi.org/10.1175/JPO2919.1>
- Racapé, V., Zunino, P., Mercier, H., Lherminier, P., Bopp, L., Pérès, F. F., & Gehlen, M. (2018). Transport and storage of anthropogenic C in the North Atlantic Subpolar Ocean. *Biogeosciences*, 15(14), 4661–4682. <https://doi.org/10.5194/bg-15-4661-2018>
- Rosón, G., Rios, A. F., Perez, F. F., Lavin, A., & Bryden, H. L. (2003). Carbon distribution, fluxes, and budgets in the subtropical North Atlantic Ocean (24.5°N). *Journal of Geophysical Research*, 108(C5), 3144. <https://doi.org/10.1029/1999jc000047>
- Sabine, C. L., Feely, R. A., Gruber, N., Key, R. M., Lee, K., Bullister, J. L., et al. (2004). The oceanic sink for anthropogenic CO<sub>2</sub>. *Science*, 305(July), 367–372. <https://doi.org/10.1126/science.1097403>
- Sallée, J. B., Matear, R. J., Rintoul, S. R., & Lenton, A. (2012). Localized subduction of anthropogenic carbon dioxide in the Southern Hemisphere oceans. *Nature Geoscience*, 5(8), 579–584. <https://doi.org/10.1038/ngeo1523>
- Sarmiento, J. L., & Gruber, N. (2002). Sinks for anthropogenic carbon. *Physics Today*, 55(8), 30–36. <https://doi.org/10.1063/1.1510279>
- Sarmiento, J. L., Orr, J. C., & Siegenthaler, U. (1992). A perturbation simulation of CO<sub>2</sub> uptake in an ocean general circulation model. *Journal of Geophysical Research*, 97(C3), 3621–3645. <https://doi.org/10.1029/91JC02849>
- Schlitzer, R. (2004). Export production in the equatorial and North Pacific derived from dissolved oxygen, nutrient and carbon data. *Journal of Oceanography*, 60(1), 53–62. <https://doi.org/10.1023/B:JOCE.0000038318.38916.e6>
- Siegel, D. A., Devries, T., Doney, S. C., & Bell, T. (2021). Assessing the sequestration time scales of some ocean-based carbon dioxide reduction strategies. *Environmental Research Letters*, 16(10), 104003. <https://doi.org/10.1088/1748-9326/ac0be0>
- Timmerman, R., Goosse, H., Madec, G., Fichefet, T., Etche, C., & Duliere, V. (2005). On the representation of high latitude processes in the ORCA-LIM global coupled sea ice-ocean model. *Ocean Modelling*, 8(1–2), 175–201. <https://doi.org/10.1016/j.ocemod.2003.12.009>
- Wang, S., Moore, J. K., Primeau, F. W., & Khattiwala, S. (2012). Simulation of anthropogenic CO<sub>2</sub> uptake in the CCSM3.1 ocean circulation-biogeochemical model: Comparison with data-based estimates. *Biogeosciences*, 9(4), 1321–1336. <https://doi.org/10.5194/bg-9-1321-2012>
- Waugh, D. W., Hall, T. M., McNeil, B. I., Key, R., & Matear, R. J. (2006). Anthropogenic CO<sub>2</sub> in the oceans estimated using transit time distributions. *Tellus Series B Chemical and Physical Meteorology*, 58(5), 376–389. <https://doi.org/10.1111/j.1600-0889.2006.00222.x>

## References From the Supporting Information

- Lueker, T. J., Dickson, A. G., & Keeling, C. D. (2000). Ocean pCO<sub>2</sub> calculated from dissolved inorganic carbon, alkalinity, and equations for K<sub>1</sub> and K<sub>2</sub>: Validation based on laboratory measurements of CO<sub>2</sub> in gas and seawater at equilibrium. *Marine Chemistry*, 70(1–3), 105–119. [https://doi.org/10.1016/S0304-4203\(00\)00022-0](https://doi.org/10.1016/S0304-4203(00)00022-0)
- van Heuven, S., Pierrot, D., Rae, J., Lewis, E., & Wallace, D. (2011). *CO<sub>2</sub>SYS, MATLAB program developed for CO<sub>2</sub> system calculations. ORNL/CDIAC-105b*. Carbon Dioxide Inf. Anal. Cent. Oak Ridge Natl. Lab.